



Magnetically separable and recyclable urchin-like Co–P hollow nanocomposites for catalytic hydrogen generation

Huizhang Guo^a, Xiang Liu^a, Yuhui Hou^b, Qingshui Xie^a, Laisen Wang^a, Hao Geng^a, Dong-Liang Peng^{a,c,*}

^a College of Materials, Xiamen University, Xiamen 361005, PR China

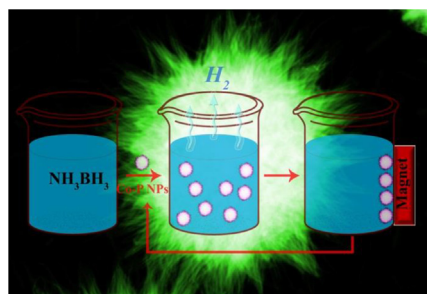
^b College of Chemistry and Chemical Engineering, Xiamen University, Xiamen 361005, PR China

^c Fujian Key Laboratory of Advanced Materials, Xiamen University, Xiamen 361005, PR China

HIGHLIGHTS

- Urchin-like Co–P hollow nanocomposites were synthesized by a one-pot strategy.
- Ferromagnetic Co nanoparticles were encapsulated into Co₂P matrix.
- The nanocomposites exhibited good catalytic hydrogen generation performance.
- The nanocomposites served as magnetic recyclable catalysts.

GRAPHICAL ABSTRACT



ARTICLE INFO

Article history:

Received 21 December 2013

Received in revised form

1 February 2014

Accepted 17 February 2014

Available online 18 March 2014

Keywords:

Hydrogen production

Co–P

Hollow nanocomposites

Magnetically recyclable

ABSTRACT

One-pot well-controlled synthetic strategy was developed to achieve urchin-like Co–P hollow nanocomposites with tailorable magnetic properties which enable them to perform as magnetically recyclable nanocatalysts in a “quasi-homogeneous” system for the catalytic hydrogen generation via hydrolysis of Ammonia–Borane (AB). The key point of this strategy was that ferromagnetic Co nanoparticles (NPs) were embedded into paramagnetic Co₂P matrix to form magnetic nanocomposites. The as-prepared Co–P NPs showed appreciable catalytic activity, recyclability and durability in hydrolysis of AB. Moreover, the chemical regeneration of AB from the “hydrolyzate” may also benefit from these magnetically recyclable catalysts. We further highlighted the excellent high-temperature resistance of Co–P NPs by calcining them at 300 °C and 600 °C. Our research may facilitate the practical application of AB as a sustainable hydrogen storage material for hydrogen-based energy.

© 2014 Elsevier B.V. All rights reserved.

1. Introduction

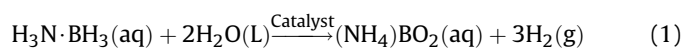
Hydrogen-based energy are supposed to hold a great potential in establishing a clean and sustainable energy system which has become a compelling demand because of the environmental pollution and dwindling fossil fuel resources. The chemical energy

storing in hydrogen can be directly converted into electrical energy in polymer electrolyte membrane fuel cell systems. Therefore, it is meaningful for us to focus the attentions in storage and conversion of hydrogen for providing safe and pure hydrogen for improving fuel cell performance with feasible cost. However, before bringing it into reality, especially for using in fuel-cell transportation, hydrogen storage is a pressing issue to be solved [1]. Ammonia–Borane (AB, NH₃BH₃) as one of the most popular representations of chemical hydrides has attracted increasing attentions because of

* Corresponding author. Tel.: +86 592 2180155; fax: +86 592 2183515.

E-mail address: dlpeng@xmu.edu.cn (D.-L. Peng).

their high hydrogen capacity (19.6 wt.%) and low molecular weight (30.7 g mol⁻¹) [2,3]. The major challenges stay behind the wide application of AB as hydrogen storage materials can be concluded as follows: 1) finding stable and recyclable catalysts; 2) relatively pure “hydrolyzate” must be generated to simplify the required chemical regeneration of AB which is a key point for using AB as sustainable fuel; 3) stable H₂ releasing with an appropriate rate even at very low temperature and concentration of AB. With these points in mind, many attentions have been focused on catalyzing release of H₂ from AB, especially, for the catalytic hydrolytic dehydrogenation of AB, as shown in Equation (1) [4–6].



Former researchers have paid more attentions in enhancing the activity and selectivity of catalysts, while the effective recovery and reuse of catalysts are usually ignored. In the homogeneous catalytic system, transition-metals have shown promise in AB dehydrogenation [7,8], but the residual metal ions in the “hydrolyzate” made the regeneration of AB quite complicated. On the other hand, in the heterogeneous catalytic system, catalysts have to be immobilized on solid support or substrate which may reduce their activity and make the dehydrogenation process expensive [9]. Recently, nanoparticles are emerging as alternatives for the immobilization of activated molecule or as catalysts themselves, which are named as “quasi-homogeneous” systems [10,11]. However, nanocatalysts usually form stable suspensions in liquid medium, as a result, intricate ultracentrifugation is required to separate the nanocatalysts from the solution after reaction. To overcome this drawback, magnetic recycle and reuse, which remove nanocatalysts from the reaction solution easily by external magnetic field, are catching researchers' attentions [12–14]. For instance, Au@Co core-shell nanoparticles [6], Au/Co/Fe triple-layered core-shell nanoparticles [15], Fe@Co core-shell nanoparticles [14] and Cu@Co [5] catalysts have been developed as magnetic recyclable nanocatalysts toward hydroboron dehydrogenation.

Meanwhile, in addition to recovery and reuse of catalysts, using earth-abundant elements and less toxic precursors are important factors in “Green Chemistry” approaches, since the stringent demands for sustainability. Previous researches have demonstrated that noble metals such as Rh [16], Ru [17] and Pt [18] possess outstanding catalytic activity toward the hydrolysis of AB. However, the practical application of these catalysts is restricted because of their high cost. Alternatively, non-noble metals [19], triple- or bi-metallic [20–22] nanocatalysts were developed, among which cobalt phosphide had shown prospects. On the other hand, the big (only) challenge with cobalt catalysts is stabilization, rather than kinetics. To establish larger structures base on smaller nanoparticles may be a promising way to enhance the stabilization.

Previous researches on cobalt phosphide synthesis have been successful in designing a variety of structures. Paul O'Brien and co-workers had synthesized single crystalline CoP nanowires by a one-pot organic route with [Co(acac)₂] (acac = acetylacetonate) and tri-n-octylphosphine oxide (TOPO) as precursors [23]. Paramagnetic Co₂P hollow spheres and tubes were prepared in Teflon-lined autoclave using traditional yellow phosphorus as phosphide sources [24]. Using Co(OA)₂ (OA = oleate) and TOPO, hyperbranched Co₂P nanostructures were fabricated in Robinson's group. [25] More recently, Co₂P nano-flowers were synthesized by thermal decomposition of Co(acac)₂ and triphenylphosphine (TPP) in Oleylamine solution, and the magnetic properties were investigated [26]. It should be noted that all of these Co₂P nanocrystals mentioned have the C₂₃ orthorhombic structure and are paramagnetic in nature, which are not suitable to be used as magnetically separable nanocatalysts discussed above. The formation of

Co₂P is a process in which reduction of Co²⁺ ions into zero valent Co atoms and phosphorization of Co atoms into cobalt phosphide occurred almost simultaneously. Since there are strong coordination effect between Co²⁺ ions and acetylacetonate ligands (Co(acac)₂ is chelate and possessing a relative large stability coefficient of LgK = 9.54), Co²⁺ ions were reduced into zero valent Co by Oleylamine or hexadecylamine at a very slow reaction rate. As a result, almost all of the Co atoms were consumed by phosphide sources immediately at an elevated temperature. Therefore, there were only paramagnetic Co₂P existing in the products.

In our recent research, Co(ac)₂ (ac = acetate) (simple coordination compound with a low stability coefficient of LgK = 1.9), in which Co²⁺ ions have a relative weak coordination with acetate ligands, is elaborately selected as cobalt precursor to react with TPP in Oleylamine solution via a one-pot organic route to form ferromagnetic Co–P nano-composited structures. In the absence of strong coordination effect from anion ligands, Co²⁺ ions were rapidly reduced into zero valent atoms by Oleylamine at high temperature. After that, urchin-like Co–P hollow nanoparticles (Co–P NPs) would form in the following aggregative growth induced by magnetostatic interaction among small Co NPs, surface phosphorization and Kirkendall effect processes. The urchin-like hollow structure makes Co–P NPs stable in AB solution as well as provides relatively large surface area for catalysis. The magnetic properties of the Co–P NPs are tailorable, which enable them to perform as magnetically recyclable catalysts for hydrogen generation via hydrolysis of AB.

2. Experimental

2.1. Chemicals

Oleylamine (80–90%) and Ammonia–Borane complex (NH₃BH₃, AB, 90%) were purchased from Acros Organics and Sigma–Aldrich, respectively. Cobalt(II) acetate tetrahydrate (Co(ac)₂·4H₂O, AR), triphenylphosphine (TPP, AR), *n*-hexane (AR), acetone (AR), ethanol (AR) were purchased from Sinopharm Chemical Reagent Co., Ltd. All of these chemicals were used as received without any further purification.

2.2. Synthesis of urchin-like Co–P hollow nanoparticles

Typically, 0.4 mmol of Co(ac)₂ and 0.8 mmol of TPP were dissolved into 7 ml Oleylamine in a 25 ml three-necked flask. After strong magnetic stirring at 100 °C with Argon purge for 20 min, the purple solution was heated up to 280 °C and refluxed at this temperature for 3 h. Then, the resulting black solution was cooled down to room temperature naturally. The black products (urchin-like Co–P hollow nanostructures) was collected by magnetic separation, and washed with a mixed solution of hexane, acetone and ethanol for several times to remove ions and possible remnants. For comparison, products were collected at different reaction time for morphological observation and magnetic property test, XPS investigation and catalytic activity test. To investigate their magnetic properties and heat resisting ability, the products were treated at 300 °C and 600 °C with a H₂ gas flow (Ar:H₂: 95:5) for one hour, which were denoted as Co–P 300 and Co–P 600, respectively. The sample without thermal treatment was denoted as Co–P RT.

2.3. Determination of the catalytic activity of urchin-like Co–P hollow nanostructures in hydrolysis of AB

The activity of Co–P catalysts in hydrolysis of AB was determined by measuring the quantity of hydrogen generation rate

using a typical water-displacement method. Before the activity test, 40 mg Co–P samples was dispersed into 10 ml water in a jacketed reaction flask (25 ml) via ultrasound concussion in an ultrasonic wave apparatus for 15 min, and then the flask was immersed into a water bath in a thermostat with a magnetic stirrer. Next, 100 mg AB was added into the catalyst solution which was stirred at 500 rpm. The hydrogen generation rate was calculated by recording the interval time cost for the displacement of per 10 ml water. Verification of the products from the catalytic reaction was performed on a mass spectrometry by infusing the generated gas into it with Ar as carrier gas.

2.4. Characterization

Power X-ray diffraction (XRD) patterns were recorded using a Panalytical X'pert PRO X-ray diffractometer with Co K α radiation operated at 40 V, 40 mA. Transmission electron microscopy (TEM) images, energy dispersive X-ray spectroscopy (EDS) data, electron diffraction patterns and elemental maps were acquired on a TECNAI F-30 transmission electron microscope equipped with a scanning TEM (STEM) unit and a high-angle annular dark-field (HAADF) detector operated at 300 kV. The SEM images were collected on a LEO 1530 scanning electron microscope operated at 20 kV. Magnetic measurements were carried out with a vibrating sample magnetometer (VSM, LakeShore 7304) at room temperature. Surface areas of the samples were determined from N $_2$ adsorption and desorption isotherms at -196°C on an automated micromeritics Tristar 2020 apparatus, using multipoint BET equation. The samples were outgassed for 3 h under vacuum at 200°C before the measurements were carried out. X-ray photoelectron spectroscopy (XPS) spectra were collected by a PHI Quantum 2000 scanning ESCA microprobe instrument to investigate the charge state. Content of phosphorus and Cobalt in each samples were determined by a JEOL JAX-8100 electroprobe micro-analyzer (EPMA).

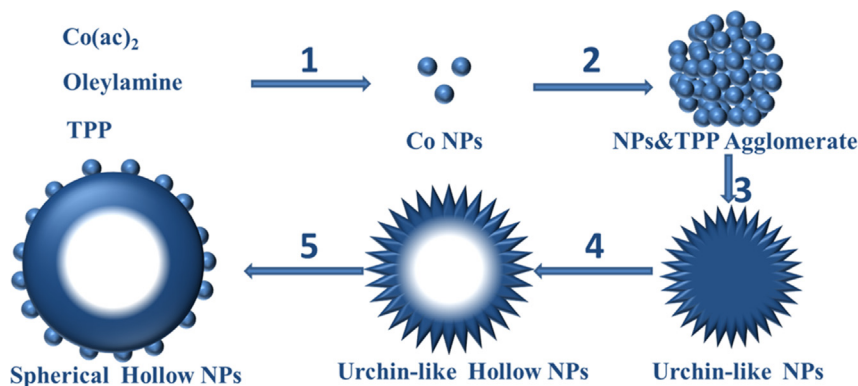
3. Results and discussion

3.1. Formation mechanism

Formation of 3D urchin-like Co–P hollow nanoparticles included a magnetic induced agglomeration among Co clusters in the initial stage and the followed surface phosphorization and Kirkendall effect on the agglomerates. Scheme 1 is a more detailed explanation of the hypothesized formation mechanism. Small Co nanoparticles (NPs) are generated via solvothermal reduction of Co(ac) $_2$ in Oleylamine solution (Scheme 1, step 1). Because of the

magnetostatic interaction among Co NPs with a scale larger than the superparamagnetic critical size, the Co NPs agglomerated together to form loosened congeries, which contained numerous nanoscale spaces filled with ligands (step 2). Actually, Co NPs congeries with ligands as space filler formed in the initial stage. Then, surface phosphorization would happen on Co congeries to form Co–P urchin-like NPs in the following aging process (step 3). It should be noted that these nanoscale spaces filled with Oleylamine played a vital role in formation of hollow structures, which slowed down the inward movement of TPP so as to compel the phosphorization occurred on the surface of Co NPs congeries preferentially. With a continuous supply of phosphorus from the decomposition of TPP, steady growth of the Co $_2$ P shell is anticipated. As the reaction proceeded, more Co atoms would diffuse outward from the inner core to react with TPP on the surface. Therefore, we can conclude that there are two major processes responsible for the creation of urchin-like hollow structures (step 4): firstly, outward diffusion of Co atoms (similar to that of Kirkendall effect); [27] secondly, phosphorization of Co on the surface to form dendritic Co $_2$ P nanostructures. In the following aging process, the outward dendritic Co $_2$ P nanostructures would gradually merge together to form a denser spherical shell. This process is similar to that of Ostwald ripening [28] and is schematically described in step 5. This denser shell may prevent the further outward diffusion of Co and encapsulate ferromagnetic Co NPs inside them. As a result, small Co NPs were encapsulated into dense Co $_2$ P matrix.

Small Co(0) nanoparticles with an average diameter of 2.2 nm can be observed if the reaction was cut off immediately when the reaction temperature reached 270°C (Fig. S1). Then, the small Co nanoparticles would grow rapidly over their superparamagnetic critical size at 280°C , and magnetic induced agglomeration among Co NPs would happen. By keeping the reaction temperature at 280°C for 2 min, polycrystalline Co NPs agglomerates with small size distribution were observed (Figs. S2 and S3). The EDX spectra indicates that there is almost no phosphorus in the product (Fig. S4). Fig. 1 compares the products at different reaction stages. A SEM image of the products generated by aging the mixed solution at 280°C for 0.5 h is presented in Fig. 1a, from which near spherical congeries of Co NPs with an average diameter of about 110 nm are observed. The corresponding TEM image shown as an insert in Fig. 1a reveals a dense structure throughout the whole congerie instead of hollow one. As the reaction time was prolonged to 1.5 h, some weeny protuberances emerged from the surface (Fig. 1b), and some voids were turning up in the center of these congeries (right insert of Fig. 1b). Near monodisperse urchin-like NPs composed of a



Scheme 1. Schematic illustration of urchin-like Co–P hollow NPs formation via one-pot process. 1) Generation of Co NPs in the initial stage; 2) Co NPs agglomerated together to form near spherical congeries induced by magnetostatic interaction; 3) surface phosphorization; 4) further phosphorization and outward diffusion of Co atoms result in the urchin-like hollow structure; 5) Ostwald ripening among the dendritic Co–P structures led to phagocytize the radial nanowires and form a compact shell.

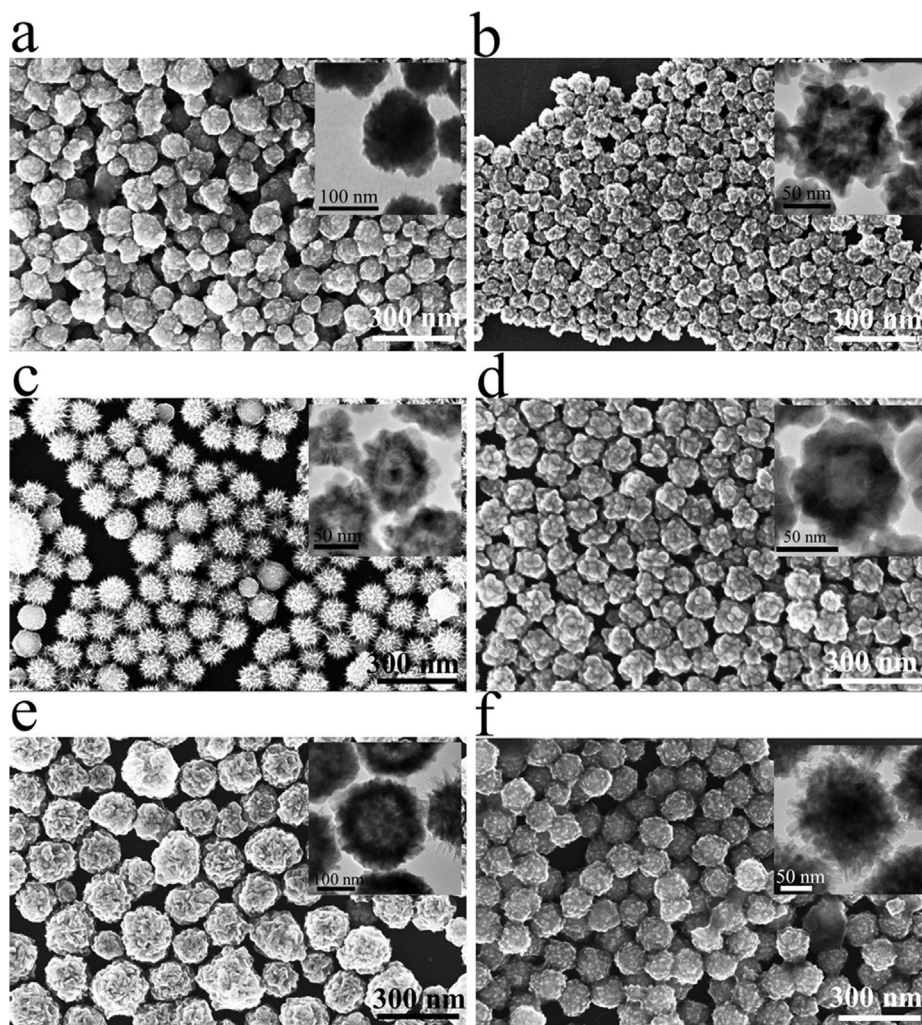


Fig. 1. a–e) Evolution of Co NPs congeries to urchin-like Co–P hollow NPs at different stages: aging at 280 °C for a) 0.5 h; b) 1.5 h; c) 2.5 h; d) 5 h; e) 10 h. f) SEM image of the products synthesized by injecting of the precursors into pre-heating Oleylamine solution (see Supplementary Information for experimental details). The insert in each figure shows the corresponding TEM image.

great deal of short dendritic structures formed after aging the mixed solution for 2.5 h (Fig. 1c). As can be expected, with a longer aging time, these voids would become larger (right insert of Fig. 1c, d and e). However, the dendritic structures dispersed gradually (Fig. 1d), and hollow NPs with dense shell were obtained (Fig. 1e), which can be attributed to Ostwald ripening. Energy dispersive X-ray spectroscopy (EDX) of these products reveals that the atomic content of phosphorus increased from 10.56 at.% for the sample generated by aging the mixed solution at 280 °C for 0.5 h to 22.56 at.% for the sample with a 2.5 h aging time. Then the content of phosphorus exhibited little change even the reaction time was prolonged to 10 h with a phosphorus content of 30.48 at.% (Fig. S5). For comparison, 2 ml of the mixed solution of TPP and $\text{Co}(\text{ac})_2$ in Oleylamine was injected rapidly into the pre-heating 7 ml Oleylamine solution at 280 °C, and then the mixed solution was kept at this temperature for 5 h. As a result, spherical NPs with homodisperse protuberances on the surface were generated (Fig. 1f), and a TEM image presented in the right insert of Fig. 1f showed a compact structure instead of hollow one. Because the rapid injection led to formation of ultra-small Co NPs [29], which were strongly agglomerated to form compact congeries encompassed almost no voids in them. As a result, a dense Co_2P shell was formed on the surface of the compact congeries and suppressed the

outward diffusion of Co at 280 °C. Therefore, it is possible for us to expect that one of the important factors attributed to the successful formation of hollow structure is that the voids filled with ligands among Co NPs in the organic-inorganic hybrid congeries promote the formation of hollow structures.

3.2. Morphology and structure

Fig. 2a displays a representative HAADF-STEM image of the urchin-like Co–P hollow NPs synthesized in the typical procedure, which demonstrates that all of the Co–P NPs are hollow with an average diameter of 110 nm. To examine the structure and composite distributions in each urchin-like Co–P hollow NP in more detail, SAED and TEM-EDS were performed on an individual Co–P NP obtained from the typical procedure. SAED pattern acquired from a single NP (right insert) demonstrates that Co–P NP is polycrystalline in nature with poor crystallinity. Elemental mapping of Co and P clearly demonstrates that both Co and P elements are almost homogeneously distributing throughout a single NP with a hollow core (Fig. 3c, d and e). The similar result was revealed by line-scan analysis across an individual particle. Accompanied these EDX analysis results with the magnetic property test which will be discussed below, we can conclude that ferromagnetic

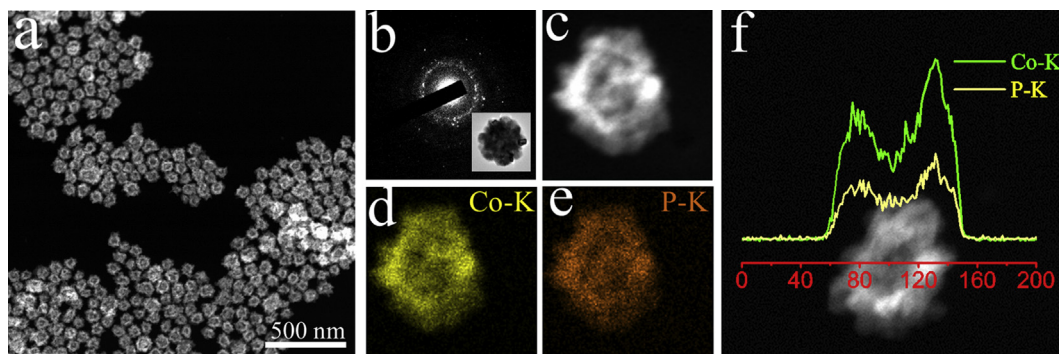


Fig. 2. a) HAADF-STEM image of the urchin-like Co–P hollow NPs synthesized in a typical procedure; b) SAED pattern acquired from a single NP (right insert); c), d) and e) HAADF-STEM image of an individual urchin like Co–P hollow NPs and corresponding EDX elemental mapping for Co (d) and P (e); f) spatial elemental distribution obtained for the EDX line-scan measurements based on Co K and P K lines.

hexagonal close packed Co NPs with tiny size were encapsulated into orthorhombic Co_2P matrix. Nitrogen adsorption–desorption results demonstrate that the Co–P NPs synthesized in the typical procedure possess a specific surface area of about $10 \text{ m}^2 \text{ g}^{-1}$ and a pore volume of $0.035 \text{ m}^3 \text{ g}^{-1}$. The IV-type Nitrogen adsorption–desorption curve (Fig. S6) indicates that the Co–P NPs are a typical of mesoporous structures. The pore size distribution curve (Fig. S6 inset) measured by Barrett–Joyner–Halenda (BJH) method shows that the Co–P NPs have a mixed mesoporous sized about 5 nm–150 nm, with an average pore diameter of about 35 nm. It reveals that beside the mesopores in the center of Co–P hollow structures which can be observed in the STEM image, there are also a large amount of tiny mesopores in the shells.

The corresponding XRD (Co K α radiation) patterns (Fig. 3) of the products at different stages indicate that all of the products are composed of hexagonal close packed Co (JCPDS: #05-0727) and orthorhombic Co_2P (JCPDS: #32-0306) phases. However, the peaks assigned to Co and Co_2P are experiencing changes in their intensity as the reaction proceeded. Specifically, the peak at 48° belonging to Co_2P became stronger as the aging time was prolonged from 0.5 h to 10 h, and the peaks at 61.78° and 65.79° which can also be assigned to Co_2P emerged once the reaction time exceeded 1.5 h. On the contrary, the peaks at 48.6° , 52.22° and 55.52° which belong to the {100}, {002} and {101} facets of Co, respectively, become weaker as the reaction continues. The change in XRD patterns demonstrates that as the aging time increased more Co atoms were consumed via phosphorization of Co atoms into Co_2P or dispersed

into Co_2P matrix. Then, the Ostwald ripening among dendritic Co_2P makes the diffraction peaks corresponding to Co_2P stronger and narrower.

Fig. 4 displays the X-ray photoelectron spectroscopy in the Co ($2p_{3/2}$) and P (2p) regions for the Co–P NPs generated in the typical procedure. All spectra were collected from the outermost layer. A couple binding energy (BE) peaks locating at 778.5 eV and 782.0 eV were observed in the Co $2p_{3/2}$ regions which were assigned to reduced Co and Co^{2+} species, respectively. The latter may results from surface oxidation. These results are consistent with former reports: the BE of non-oxidic Co $2p_{3/2}$ in Co_2P was 778.2 eV, the BE of Co^{2+} in Co $2p_{3/2}$ was 782.4 eV [30]. A similar result can be observed in the Co $2p_{1/2}$ regions (Fig. S7), which displays a couple of peaks at 794.2 eV and 797.7 eV, respectively. The one peaking at 764.2 eV that is assigned to reduced Co shows a slight shift to high energy region, which may owe to the partly transfer of electrons from reduced Co to P. On the other hand, there are three peaks at 129.7, 130.8 and 133.5 eV in P 2p region. The peak at 129.7 eV can be referred to reduced P in Co_2P which is similar to that reported before [30], while the one locating at 133.5 eV was assigned to P^{5+}

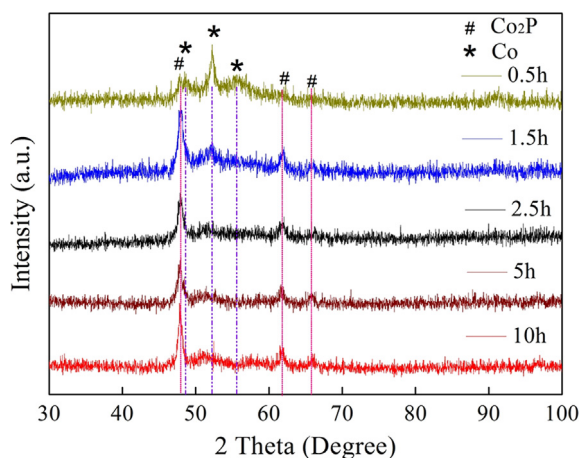


Fig. 3. XRD patterns of the products at different reaction stages.

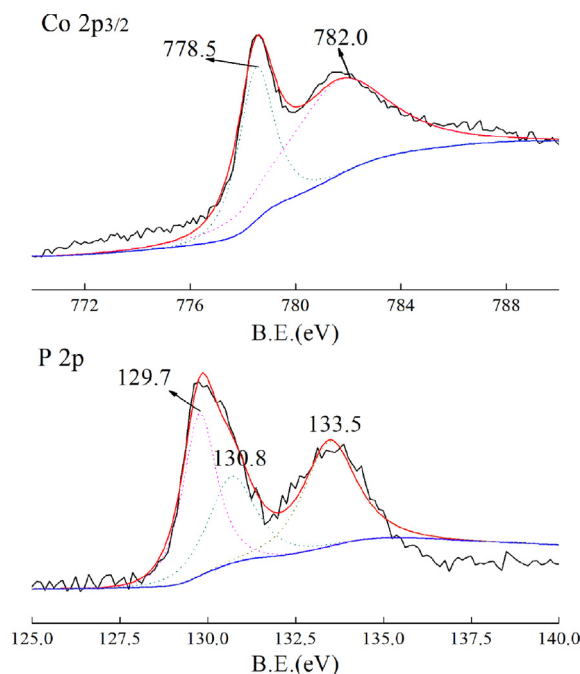


Fig. 4. XPS spectra of Co–P NPs.

species [31] which may present in the form of PO_4^{3-} owing to surface oxidation as well. It should be noted that there is another peak at 130.8 eV which is very close to the BE of P in organometallic compound, such as $\text{Pt}(\text{P}(\text{C}_6\text{H}_5)_3)_4$ (131.3 eV), [32] $(\text{C}_5\text{H}_4\text{P}(\text{C}_6\text{H}_5)_2)_2\text{Fe}$ (130.9 eV) [33]. Therefore, the presence of the BE at 130.8 eV reveals that TPP was adsorbing on the surface of Co–P NPs. In accordance with what we have discussed above, the surface adsorption of TPP is very important for the further phosphorization and Kirkendall effect.

3.3. Magnetic property

Field dependent magnetization of the samples generated with different reaction time was investigated at room temperature, and the analytical results accompanied with phosphorus contents were summarized in Table S1. As shown in Fig. 5a, the saturation magnetization of Co–P NPs experienced a gradually decline as the aging time prolonged. Specifically, the saturation magnetization of Co–P 0.5 h was about 39.31 emu g^{-1} , which declines to 4.07 emu g^{-1} for Co–P 10 h. According to former researches [26,34], Co_2P with C_{23} orthorhombic structure exhibits Curie–Weiss paramagnetic behavior. As the reaction processing, phosphorus content experienced a gradually increase (Table S1). In other word, ferromagnetic phase (hexagonal Co) was consumed to form a paramagnetic phase (C_{23} orthorhombic Co_2P) in this aging procedure. On the other hand, there was no obvious change in the coercivity of the three samples, which is about 300 Oe for the samples generated by aging for 0.5 h, 2.5 h or 10 h in the typical procedure. These results reveal that it is facile for us to tailor the magnetization while

keep their coercivity almost unchanged. The tailor-able saturation magnetization of Co–P NPs will benefit them for recovery and reuse after catalytic reactions which are vital for sustainable process management [9]. Meanwhile, their relative low coercivity may avoid them from aggregation caused by magnetostatic interaction.

3.4. Thermostability of the urchin-like Co–P hollow NPs

In order to test their thermostability, urchin-like Co–P hollow NPs synthesized at 280°C for 3 h in the typical procedure were treated at 300°C and 600°C with a H_2 gas flow ($\text{Ar}:\text{H}_2$: 95:5) for one hour, which were named as Co–P 300 and Co–P 600, respectively. The sample without thermal treatment was denoted as Co–P RT. As determined by N_2 adsorption and desorption isotherms at 77 K, the BET surface area of Co–P RT is about $10 \text{ m}^2 \text{ g}^{-1}$. It should be noted that there is not obvious change in the surface area of Co–P 300 or Co–P 600, which are $10.25 \text{ m}^2 \text{ g}^{-1}$ and $9.78 \text{ m}^2 \text{ g}^{-1}$, respectively (Table S2). The HAADF-STEM image of the Co–P 600 after being exposed in air for a couple days displays dispersed Co–P NPs without serious aggregation or deformation in their morphology. Nitrogen adsorption–desorption and pore size distribution curves revealed that Co–P NPs still hold the mesoporous structures with a main pore size of about 35 nm (Fig. S8). From the STEM image, no collapsed structure formed after being calcined at 600°C (Fig. S9). It indicates that the as-prepared urchin-like Co–P hollow NPs possess excellent high temperature stability, even at a temperature of 600°C . The saturation magnetization climbed from 18.3 emu g^{-1} to 26.5 emu g^{-1} after the heat treatment at 300°C (Fig. 5b and Table S2), which may result from the reduction of oxidic Co^{2+} into ferromagnetic Co. However, this value declined to 5.1 emu g^{-1} for Co–P 600. Almost all of the surfactants such as Oleylamine and TPP were decomposed and a deeper phosphorization process had occurred at the temperature higher than 300°C . In addition, serious oxidation would occur to form oxides (such as cobaltous phosphate) after exposing in air. As can be seen from the high magnification HAADF-STEM image acquired from an individual particle (Fig. S10), there was a low contrast shell covering on the surface of Co–P NP. It demonstrated that the surface layer of Co–P NPs had been seriously oxidized because of the absence of capping agents, which can be evidenced by the XPS spectra collected from the outer layer of Co–P 600. As shown in Fig. S11, the peak locating at 130.8 eV belonging to TPP disappeared. More importantly, the peak belongs to P^{5+} (133.5 eV) displays a larger area than the one corresponding to reduced P (129.7 eV), which is contrary to Co–P RT shown in Fig. 5b.

3.5. Hydrogen generation kinetics

In order to show that the Co–P catalysts might have utilization in hydrogen industry, we evaluated their catalytic activities for the hydrolytic dehydrogenation of AB which is a promising chemical hydrogen storage material. Fig. 6a shows the hydrogen generation kinetics under the catalysis of 12 mg and 40 mg Co–P 300 catalysts, which have the highest magnetization and excellent dispersibility in water. The hydrolysis reaction is completed in a shorter time in the presence of more Co–P NPs. However, the hydrogen generation rates are almost equal to each other if they are presented in the unit of $\text{ml min}^{-1} \text{ g}^{-1}$ (which is actually the sort of TOF), which is $1749 \text{ ml min}^{-1} \text{ g}^{-1}$ with 40 mg Co–P 300 and $1820 \text{ ml min}^{-1} \text{ g}^{-1}$ with 12 mg Co–P 300, respectively. Fig. 6b shows the variation of hydrogen generation rate with different initial AB concentration in 10 g DI water at 25°C in the presence of 40 mg Co–P 300 catalysts. As the initial AB concentration rises from 0.2 wt.% to 1 wt.%, hydrogen generation rate increased from $1092 \text{ ml min}^{-1} \text{ g}^{-1}$ to $1749 \text{ ml min}^{-1} \text{ g}^{-1}$. It was found that the yield of hydrogen

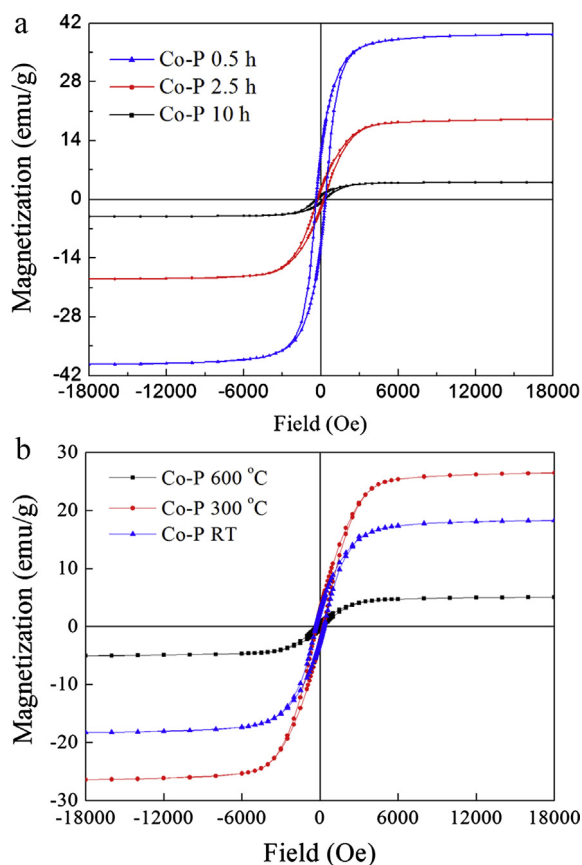


Fig. 5. a) Field dependence magnetization curves of urchin-like Co–P hollow NPs prepared with different reaction time in the typical procedure (0.5 h, 2.5 h, 10 h); b) field dependence magnetization curves of Co–P RT, Co–P 300 and Co–P 600.

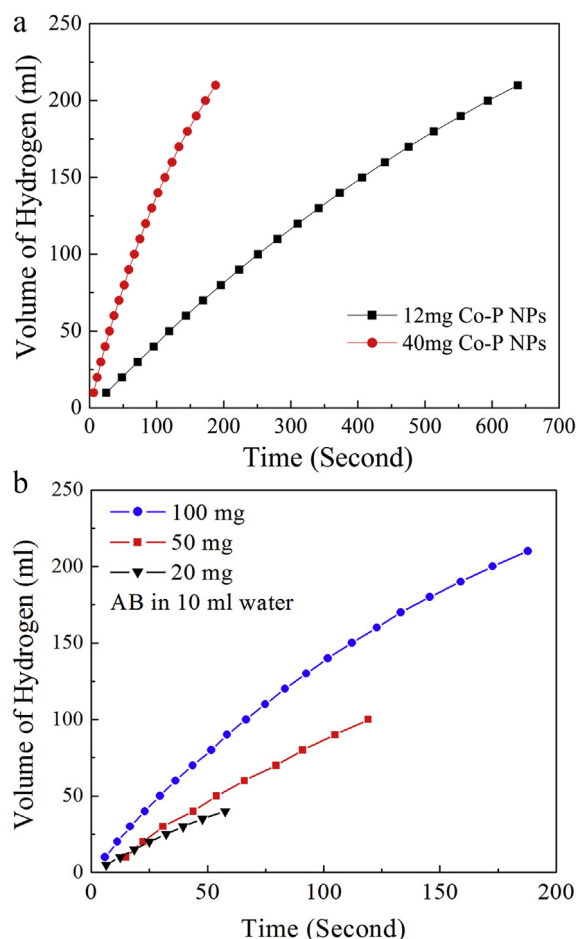


Fig. 6. a) Hydrogen generation kinetics under the catalysis of 40 mg (red) and 12 mg Co–P 300 (black) at 25 °C in 10 ml 1 wt.% AB solution; b) hydrogen generation kinetics at 25 °C under the catalysis of 40 mg Co–P 300 in 1 wt.% (blue), 0.5 wt.% (red) and 0.2 wt.% (black) AB solution. (For interpretation of the references to color in this figure legend, the reader is referred to the web version of this article.)

production (H_2/AB) was independent of AB concentration, although the hydrogen generation rates were varying with different initial AB loading in equal water. In other word, full AB conversion efficiency could be obtained for all concentration of AB with stable hydrogen generation rates throughout the hydrolysis reaction. It should be noted that the slight curve observed in Fig. 6 may owe to the decline in the liquid level as the water was replaced by hydrogen as the reaction proceed in the typical water-displacement method. These results indicate that hydrolysis of AB under the catalysis of Co–P NPs is a zero order reaction. For comparison, hydrogen generation rate at 25 °C under the catalysis of 40 mg Co–P NPs prepared by aging for 10 h was collected. The result indicates that there is almost no change in hydrogen generation rate either in the catalysis of Co–P NPs 3 h or Co–P NPs 10 h. Our mass spectrometry analysis suggested that the generated gas was pure H_2 without any other impurity such as NH_3 detected throughout the catalytic reaction (see Figs. S12 and S13 for the experimental results).

The hydrogen generation rate predominantly depends on the temperature. Fig. 7a displays the influence of reaction temperature on the hydrogen generation kinetics under the catalysis of 40 mg Co–P 300 in 1 wt.% AB solution. As the reaction temperature rose from 5 °C to 25 °C, the hydrogen generation rates increased from 525 $ml\ min^{-1}\ g^{-1}$ to 1749 $ml\ min^{-1}\ g^{-1}$ (Fig. 7b). It reveals that a stable hydrogen supply is possible even at a relatively low

temperature (5 °C). Furthermore, the reaction rates keep almost constant throughout the reaction at any given temperature, even though the concentration of AB may decrease as the reaction proceeding. These indicate that the catalytic generation of hydrogen by hydrolysis of AB is a zero-order reaction [9,20,35]. In other word, the activation energy (E_a) is independent of reaction temperature. As a result, the Arrhenius' reaction rate equation can be presented as the following form:

$$\ln(v_r) = \ln k_0 + \frac{-E_a}{RT} \quad (2)$$

in which v_r is reaction rate ($ml\ min^{-1}\ g^{-1}$), k_0 is the reaction constant ($ml\ min^{-1}\ g^{-1}$), E_a is the activation energy for the reaction, while R and T is gas constant and reaction temperature (Kelvin), respectively. Fig. 7b displays the Arrhenius plot in which $\ln(v_r)$ is plotted versus the reciprocal of absolute temperature ($1/T$), from which the activation energy for the hydrolysis of AB in the catalysis of Co–P 300 catalysts is calculated to be 41 $kJ\ mol^{-1}$ by Equation (2). Meanwhile, we also studied the hydrogen generation kinetics under the catalysis of 40 mg Co–P RT in 1 wt.% AB solution. Compared with Co–P 300, Co–RT catalysts have a lower hydrogen generation rate under the same conditions. To be specific, the hydrogen generation rate increased from 367 $ml\ min^{-1}\ g^{-1}$ to 1051 $ml\ min^{-1}\ g^{-1}$ as the reaction temperature rose from 5 °C to 25 °C (Fig. 7c). The lower hydrogen generation rate of Co–P RT catalysts may owe to their poor dispersibility in water, because the surface of Co–P RT NPs was covered by the hydrophobic ligands such as Oleylamine and TPP. However, the activation energy for the hydrolysis of AB in the catalysis of Co–P RT was calculated to be 34.6 $kJ\ mol^{-1}$ (Fig. 7d), which is a little lower than that of Co–P 300. Although, activation energy of the urchin-like Co–P hollow NPs is higher than some of the supported noble metal-based catalysts [36], it is less than many non-noble metal-based catalysts (Table S3), such as Co/r- Al_2O_3 (62 $kJ\ mol^{-1}$), [37] NiAg (51.5 $kJ\ mol^{-1}$), [21] and the more recent Cu–Co catalysts ($\sim 1000\ ml\ min^{-1}\ g^{-1}$ at ambient temperature) prepared via Layered double hydroxides [5].

Moreover, the point is that the as-prepared urchin-like Co–P hollow NPs possess high durability and easy magnetic recyclability owing to their high magnetization. During the catalytic reaction, Co–P 300 catalysts were suspended in AB aqueous solution to provide a large surface area for the hydrolysis reaction (Fig. S14a). And then the magnetic catalysts can be easily separated from the solution via external magnetic field after reaction (Fig. S14b). The magnetic recyclable process avoids leaving the residual catalysts in the “hydrolyzate”, which may make the regeneration of AB facile. The durability of Co–P 300 catalysts were determined by dispersing the catalysts in 10 ml water via sonication before 100 mg AB was poured into the reactor, after the completion of hydrolytic reaction Co–P catalysts were magnetically separated from the mother liquor for the next cycle. The durability tests were carried out one cycle per 3 days, and catalysts were immersing in the mother liquor under ambient condition during the time between every two cycles. As can be seen in Fig. 8, the Co–P NPs maintained their initial catalytic activity even in the 7th run after being kept in the solution for 21 days. There was also not obvious change in the morphology of the reused catalysts observed from the TEM image (Fig. S15).

4. Conclusion

In summary, urchin-like Co–P hollow NPs were synthesized in a one-pot well-controlled procedure in organic solution. The saturation magnetization of these Co–P NPs could be facily controlled

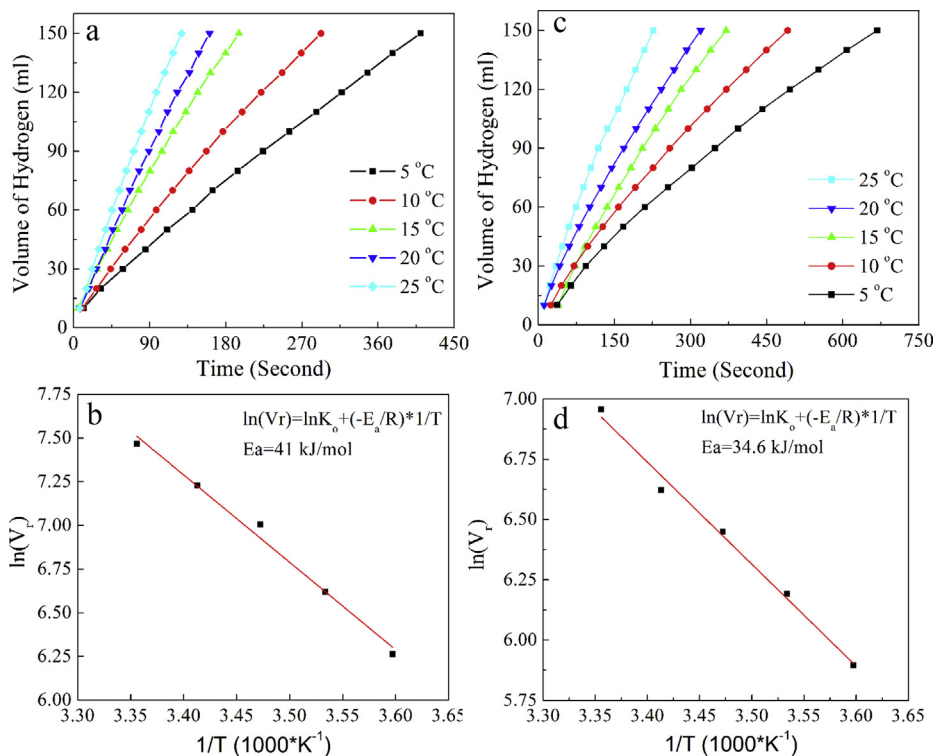


Fig. 7. a) and c) Effect of temperature variation on hydrogen generation kinetics under the catalysis of 40 mg Co–P 300 and Co–P RT in 1 wt.% AB solution; b) and d) Arrhenius plots obtained from the data shown in a) and c), respectively.

in a wide range, from 39.48 emu g^{-1} to 5.05 emu g^{-1} . An appreciable catalytic activity for hydrogen generation by hydrolysis of AB was achieved, which is comparable to most of the noble metal-based catalysts. The urchin-like hollow structure makes Co–P NPs stable in solution and provides relatively large surface area for catalysis. The unique magnetic features of the Co–P NPs enable them to perform as magnetically recyclable nanocatalysts which possess outstanding recyclability and durability in hydrolysis of AB. Furthermore, the magnetic separable catalytic process avoids leaving the residual catalysts in the “hydrolyzate”, which facilitate the regeneration of AB. The as-prepared Co–P NPs also showed excellent high-temperature resistance. We supposed that our research

may facilitate the practical application of AB as hydrogen storage materials and make the hydrogen energy conversion more “Green”.

Acknowledgments

The authors gratefully acknowledge financial support from the National Basic Research Program of China (no. 2012CB933103), the National Outstanding Youth Science of China (no. 50825101), the National Natural Science Foundation (51171158). We thank Mingxiang Huang and Jiashu Chen for their helpful discussion.

Appendix A. Supplementary data

Supplementary data related to this article can be found at <http://dx.doi.org/10.1016/j.jpowsour.2014.02.067>.

References

- [1] P. Chen, M. Zhu, *Mater. Today* 11 (2008) 36–43.
- [2] F.H. Stephens, V. Pons, R. Tom Baker, *Dalton Trans.* (2007) 2613–2626.
- [3] T.B. Marder, *Angew. Chem. Int. Ed.* 46 (2007) 8116–8118.
- [4] Ö. Metin, V. Mazumder, S. Özkur, S. Sun, *J. Am. Chem. Soc.* 132 (2010) 1468–1469.
- [5] C. Li, J. Zhou, W. Gao, J. Zhao, J. Liu, Y. Zhao, M. Wei, D.G. Evans, X. Duan, *J. Mater. Chem. A* 1 (2013) 5370–5376.
- [6] J.-M. Yan, X.-B. Zhang, T. Akita, M. Haruta, Q. Xu, *J. Am. Chem. Soc.* 132 (2010) 5326–5327.
- [7] T.J. Clark, C.A. Russell, I. Manners, *J. Am. Chem. Soc.* 128 (2006) 9582–9583.
- [8] M.C. Denney, V. Pons, T.J. Hebdon, D.M. Heinekey, K.I. Goldberg, *J. Am. Chem. Soc.* 128 (2006) 12048–12049.
- [9] K. Eom, K. Cho, H. Kwon, *Int. J. Hydrogen Energy* 35 (2010) 181–186.
- [10] D. Wang, Y. Li, *Adv. Mater.* 23 (2011) 1044–1060.
- [11] S. Shylesh, V. Schünemann, W.R. Thiel, *Angew. Chem. Int. Ed.* 49 (2010) 3428–3459.
- [12] A.-H. Lu, E.L. Salabas, F. Schüth, *Angew. Chem. Int. Ed.* 46 (2007) 1222–1244.
- [13] M.B. Gawande, P.S. Branco, R.S. Varma, *Chem. Soc. Rev.* 42 (2013) 3371–3393.
- [14] C.W. Tsai, H.M. Chen, R.S. Liu, J.F. Lee, S.M. Chang, B.J. Weng, *Int. J. Hydrogen Energy* 37 (2012) 3338–3343.

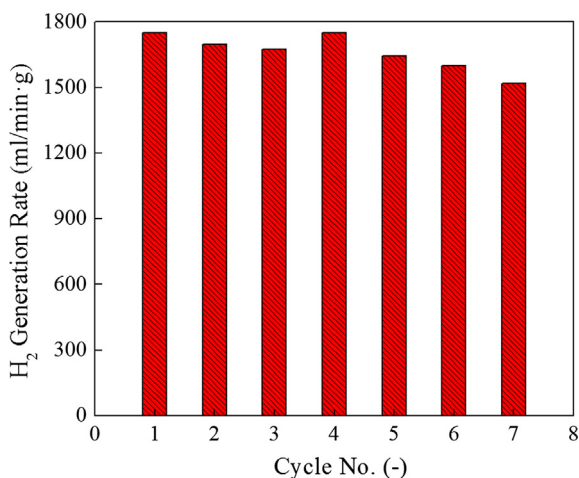


Fig. 8. Evolution of hydrogen generation rate as a function of cycle times (one cycle per 3 days), at 25 °C in 10 ml 1 wt.% AB solution using 40 mg Co–P 300 catalysts.

- [15] K. Aranishi, H.-L. Jiang, T. Akita, M. Haruta, Q. Xu, *Nano Res.* 4 (2011) 1233–1241.
- [16] M. Zahmakıran, S. Özkar, *Appl. Catal. B Environ.* 89 (2009) 104–110.
- [17] S. Basu, A. Brockman, P. Gagare, Y. Zheng, P.V. Ramachandran, W.N. Delgass, J.P. Gore, *J. Power Sources* 188 (2009) 238–243.
- [18] N. Mohajeri, A. T-Raissi, O. Adebisi, *J. Power Sources* 167 (2007) 482–485.
- [19] Ö. Metin, S. Özkar, S. Sun, *Nano Res.* 3 (2010) 676–684.
- [20] J.C. Ingersoll, N. Mani, J.C. Thenmozhiyal, A. Muthaiah, *J. Power Sources* 173 (2007) 450–457.
- [21] C.F. Yao, L. Zhuang, Y.L. Cao, X.P. Ai, H.X. Yang, *Int. J. Hydrogen Energy* 33 (2008) 2462–2467.
- [22] B.H. Liu, Z.P. Li, S. Suda, *J. Alloys Compd.* 415 (2006) 288–293.
- [23] Y. Li, M.A. Malik, P. O'Brien, *J. Am. Chem. Soc.* 127 (2005) 16020–16021.
- [24] H. Hou, Q. Peng, S. Zhang, Q. Guo, Y. Xie, *Eur. J. Inorg. Chem.* 2005 (2005) 2625–2630.
- [25] H. Zhang, D.-H. Ha, R. Hovden, L.F. Kourkoutis, R.D. Robinson, *Nano Lett.* 11 (2010) 188–197.
- [26] N. Zhang, A. Shan, R. Wang, C. Chen, *CrystEngComm* 14 (2012) 1197–1200.
- [27] Y. Yin, R.M. Rioux, C.K. Erdonmez, S. Hughes, G.A. Somorjai, A.P. Alivisatos, *Science* 304 (2004) 711–714.
- [28] S. Xiong, H.C. Zeng, *Angew. Chem. Int. Ed.* 51 (2012) 949–952.
- [29] A.R. Tao, S. Habas, P. Yang, *Small* 4 (2008) 310–325.
- [30] T.I. Korányi, *Appl. Catal. A Gen.* 239 (2003) 253–267.
- [31] P.J. Mangnus, J.A.R. Van Veen, S. Eijssbouts, V.H.J. De Beer, J.A. Moulijn, *App. Catal.* 61 (1990) 99–122.
- [32] Y.M. Shul'ga, A.V. Bulatov, R.A.T. Gould, W.V. Konze, L.H. Pignolet, *Inorg. Chem.* 31 (1992) 4704–4706.
- [33] T.S.A. Hor, H.S.O. Chan, K.L. Tan, L.T. Phang, Y.K. Yan, L.K. Liu, Y.S. Wen, *Polyhedron* 10 (1991) 2437–2450.
- [34] S. Fujii, S. Ishida, S. Asano, *J. Phys. F Met. Phys.* 18 (1988) 971.
- [35] S.C. Amendola, S.L. Sharp-Goldman, M.S. Janjua, M.T. Kelly, P.J. Petillo, M. Binder, *J. Power Sources* 85 (2000) 186–189.
- [36] M. Chandra, Q. Xu, *J. Power Sources* 168 (2007) 135–142.
- [37] Q. Xu, M. Chandra, *J. Alloys Compd.* 446–447 (2007) 729–732.